

# A 30 AU radius CO gas hole in the disk around the Herbig Ae star Oph IRS 48<sup>1</sup>

J.M. Brown<sup>1,2</sup>, G.J. Herczeg<sup>1</sup>, K.M. Pontoppidan<sup>3</sup>, E.F. van Dishoeck<sup>1,4</sup>

## ABSTRACT

The physical processes leading to the disappearance of disks around young stars are not well understood. A subclass of transitional disks, the so-called cold disks with large inner dust holes, provide a crucial laboratory for studying disk dissipation processes. IRS 48 has a 30 AU radius hole previously measured from dust continuum imaging at 18.7  $\mu\text{m}$ . Using new optical spectra, we determine that IRS 48 is a pre-main sequence A0 star. In order to characterize this disk's gas distribution, we obtained AO-assisted VLT CRIRES high resolution ( $R \sim 100,000$ ) spectra of the CO fundamental rovibrational band at 4.7 micron. All CO emission, including that from isotopologues and vibrationally excited molecules, is off-source and peaks at 30 AU. The gas is thermally excited to a rotational temperature of 260 K and is also strongly UV pumped, showing a vibrational excitation temperature of  $\sim 5000$  K. We model the kinematics and excitation of the gas and posit that the CO emission arises from the dust hole wall. Prior imaging of UV-excited PAH molecules, usually a gas tracer, within the hole makes the large CO hole even more unexpected.

*Subject headings:* stars: pre-main-sequence — (stars:) planetary systems: protoplanetary disks — stars: individual (Oph IRS 48)

---

<sup>1</sup>Max-Planck-Institut für extraterrestrische Physik, Postfach 1312, 85741 Garching, Germany ; joannabrown@cfa.harvard.edu

<sup>2</sup>Harvard-Smithsonian Center for Astrophysics, 60 Garden St., MS 78, Cambridge, MA 02138

<sup>3</sup>Space Telescope Science Institute, 3700 San Martin Drive, Baltimore, MD 21218

<sup>4</sup>Leiden Observatory, P.O. Box 9513, NL-2300 RA Leiden, The Netherlands

<sup>1</sup>This work is based on observations collected at the European Southern Observatory Very Large Telescope under program ID 179.C-0151.

## 1. Introduction

Disk around pre-main sequence stars are the birthsites of planets, yet many questions remain about the formation processes of planets and the end stages of the disk. Planets are expected to leave distinctive gaps in the disk as they clear their orbital paths (Artymowicz & Lubow 1994; Bryden et al. 1999; Crida & Morbidelli 2007). Transitional disks, in which dust clearing has begun in the inner regions, may be the predicted objects (e.g. Strom et al. 1989; Calvet et al. 2002; Brown et al. 2007; Najita et al. 2007). A young substellar candidate recently discovered in the transitional disk T Cha lends credence to this hypothesis (Huélamo et al. 2011). However, dust deficits in spectral energy distributions (SEDs) can potentially result from other processes including photoevaporation and grain growth. Gas observations can help to distinguish between these scenarios. Gas and dust are removed near simultaneously in inside-out disk photoevaporation models and would have similar distributions (Alexander et al. 2006; Owen et al. 2011). At the other extreme, the creation of an apparent dust hole through grain growth and settling would cause no depletion of the gas. Finally, stellar and planetary companions can clear gaps free of both gas and dust, but some movement of material across these gaps would be expected depending on companion size and location (Artymowicz & Lubow 1996; Zhu et al. 2011). The creation of gaps by companions can enhance other avenues of disk clearing such as photoevaporation (Alexander & Armitage 2009). Gas observations are also of particular relevance in the case of young planets as the gas drives both formation and migration.

CO rovibrational emission is sensitive to warm  $\sim 100$ - $1000$  K gas and is commonly seen from young disks around both Herbig Ae/Be (e.g. Blake & Boogert 2004) and T Tauri stars (Najita et al. 2003). These lines are particularly useful as tracer of gas for transition disks as the  $\sim 1000$  K gas temperatures and high velocities likely imply gas within the dust holes (Salyk et al. 2009). Spectroastrometric observations of three transition disks confirm that the CO fundamental emission generally traces gas within the dust holes but in one case a 7 AU gas hole within a  $\sim 30$  AU dust hole was found (Pontoppidan et al. 2008). Lack of CO fundamental emission from the inner regions of Herbig Ae/Be stars appears slightly more common with a handful of disks currently known: HD 141569A (11 AU radius gas hole, Goto et al. 2006), HD 97084 and HD 100546 (11 and  $>8$  AU radii respectively, van der Plas et al. 2009). Brittain et al. (2007, 2009) successfully modeled the emission distributions in both HD 141569A and HD 100546 with UV-fluorescent gas. Pontoppidan et al. (2011a) finds that it is natural for higher luminosity sources to have larger inner CO-free regions, although some sources have even larger inner holes than expected.

The radiative environment around young high mass stars is harsher than around T Tauri stars and allows investigation of disk dissipation processes under different conditions. The

majority of transitional disks found to date surround G-type and later stars, although dust holes are seen at all stellar masses. Many factors might be responsible for the lower numbers including the rarity of local Herbig Ae/Be stars, the potential for a faster transition timescale, and difficulty in identifying transition disks around higher mass stars. Herbig Ae/Be SEDs have traditionally been classified into almost flat SEDs (group I) and those with a strong decline in the far-infrared (group II) (Meeus et al. 2001; Hillenbrand et al. 1992). These classes represent flared and self-shadowed disks (Dullemond & Dominik 2004), although the transition between the two is likely continuous (Meijer et al. 2008). The high luminosities of these stars are capable of producing puffed-up inner rims which shadow the disk behind (Dullemond & Dominik 2004; Acke et al. 2009) and can produce SEDs qualitatively similar to transition disk SEDs due to the difficulty in distinguishing between shadowed and missing material. However, dust holes are present in disks around at least some higher mass sources with millimeter imaging of MWC 758 (A8) and HD 135344B (F4) clearly resolving dust cavities (Andrews et al. 2011; Brown et al. 2009). Exoplanets have also been directly imaged around older high mass stars at distances that could explain large inner holes (e.g. Marois et al. 2008) implying that their younger precursors may be transition disks.

The Herbig Ae star IRS 48 in  $\rho$  Ophiuchi star formation region has an unusual disk. It was first noted for its strong PAH emission and implied strong UV field. Spatially resolved mid-IR images of the dust reveal a ring-like structure at  $18.7 \mu\text{m}$  with a distance of 110 AU between the brightness peaks and an inner dust hole with a radius of  $\sim 30$  AU (Geers et al. 2007). A strong east-west directionality is seen leading Geers et al. (2007) to conclude a disk inclination of  $48^\circ \pm 8^\circ$ . Strong polycyclic aromatic hydrocarbon (PAH) molecular emission, likely tracing gaseous molecular material, was found to be centered on the star and fill in this large grain ring. The CO gas might be expected to have a similar distribution to the PAHs and be present inside the dust hole. The VLT-CRIRES spectrograph offers the combination of spectral and spatial resolution to resolve the warm gas in this disk. In this paper, we present CRIRES observations of IRS 48 showing spatially extended CO rovibration emission and examine both the kinematics and excitation to determine the gas structure and origin.

## 2. Observations

### 2.1. CRIRES

We observed Oph IRS 48 (WLY 2-48,  $\alpha = 16^{\text{h}}27^{\text{m}}37^{\text{s}}.19$ ,  $\delta = -24^\circ 30' 34''.8$ , J2000) with CRIRES in the M band ( $4.63\text{--}4.87 \mu\text{m}$ ) covering the CO fundamental rovibrational band as part of a large CRIRES program studying a sample of  $\sim 100$  stars (Pontoppidan et al. 2011b). CRIRES is a cryogenic echelle spectrograph behind the Multi-Application Curvature

Adaptive Optics (MACAO) system on the 8m VLT 1, Antu (Kaeufl et al. 2004). A slit width of  $0''.2$  was used to provide a resolving power of  $R \sim 100,000$  ( $\Delta v = 3 \text{ km s}^{-1}$ ). The observations were taken on several different dates in 2007 and 2008 (see Table 1).

The data were reduced following the procedures of Pontoppidan et al. (2008). The data were taken with an ABBA  $10''$  dithered nodding pattern permitting a first order correction of the infrared background by pair subtraction. Integration times for each position were 1 minute leading to 4 minute nod cycles. The number of nod cycles in each setting is listed in Table 1. The CRIRES pixel scale was 86 mas which was subdivided during reduction into 43 mas/pixel. The 2-D spectra were linearized and then extracted. The spatially extended emission required customized extraction. For an overall spectrum, an aperture of  $1''.2$  was used to include all extended emission. Spectra were also extracted in 2 pixel (86 mas) apertures to produce a spectral map. All spectra were wavelength calibrated using the strong telluric features in the standard star spectra. The standard stars all have spectral types of O or B, chosen for their lack of spectral features in the M band. Finally, the many weak telluric features were removed by dividing the source spectra by the standard star spectra. Remaining strong telluric features with transmission of  $<20\%$  were blanked from the analyzed spectra.

The majority of the observations were taken with the slit at a position angle of  $90^\circ$ , following the east-west directionality seen in the Geers et al. (2007) images. Spectra at  $0^\circ$  and  $180^\circ$  were also taken to examine the orthogonal distribution of the CO emission (see Table 1).

Flux calibration was done by normalizing to Spitzer IRAC fluxes. Calibration directly from the M-band standard star spectra suffers from variable throughput effects, but in this case, direct flux calibration was within 20% of the Spitzer IRAC fluxes. We therefore have reasonable confidence that the  $5 \mu\text{m}$  continuum flux has not changed significantly since the Spitzer observations.

## 2.2. Spectral type of IRS 48

The spectral type of IRS 48 is unclear from the literature. Luhman & Rieke (1999) found a spectral type earlier than F3 from a K-band spectrum. In contrast, Geers et al. (2007) argued for M0 based on an optical spectrum obtained with a fiber-fed multi-object spectrograph. However, telluric  $\text{H}_2\text{O}$  absorption in the optical spectrum may have been mistaken for the  $\text{TiO}$  band absorption characteristic of M0 stars.

To resolve this discrepancy, we obtained a flux-calibrated, low-resolution ( $R \sim 1000$ )

optical spectrum using LRIS-ADC on Keck I (Oke et al. 1995) on 2008 May 28. Although the observation spans 3000–9300 Å, the star is only detected longward of 5500 Å because of extinction. Some weak H $\alpha$  emission is tentatively detected in our spectrum and in the Geers et al. (2007) spectrum, likely indicating the presence of accretion and consequently gas in the inner disk (Muzerolle et al. 2004). Pfund- $\beta$  emission is also detected in the CRIRES spectra, another probable indicator of accretion. The presence and relative strength of absorption in the H Paschen and Ca II IR triplet lines clearly indicate that IRS 48 is an A-type star, consistent with the Br- $\gamma$  absorption detected by Luhman & Rieke (1999). By comparison with the Pickles (1998) stellar spectral flux library, we assign a spectral type of A0 $_{-1}^{+4}$  to IRS 48, which corresponds to an effective temperature of 9000 $\pm$ 550 K (Figure 1).

The extinction is estimated by comparing the continuum slope in our optical spectrum to the continuum slopes of early A-type stars in Pickles (1998). The extinction curve used is that of Weingartner & Draine (2001) for  $R_V = 5.5$ , which approximates the opacity of large dust grains that are thought to be typical of dense star-forming regions (Indebetouw et al. 2005). We measure  $A_V = 11.50 \pm 0.25$  mag, confirming the presence of substantial intervening material in the line of sight, as is common in Ophiuchus.

Based on the spectral type, extinction, a J-band magnitude of 10.57 (Skrutskie et al. 2006), and a distance of 120 pc to  $\rho$  Oph (Loinard et al. 2008), the stellar luminosity is 14.3  $L_\odot$ . The Siess et al. (2000) evolutionary tracks then imply that IRS 48 is a  $\sim 2.0 M_\odot$  star with an age of  $\sim 15$  Myr at the start of the main sequence. The spectral type and luminosity are inconsistent with the 1 Myr age that is typically measured for Ophiuchus. At 1 Myr, a star with spectral type A0 would have a luminosity of  $\sim 200 L_\odot$  and a mass of  $\sim 4.5 M_\odot$ . Potential sources of error in the calculated luminosity could be a high gray extinction and scattering off an edge-on disk, the dust opacity ( $R_V=5.5$ ) used in the extinction correction or the distance, which would likely exclude membership in Ophiuchus. We discuss this discrepancy further in Section 6, including additional constraints from the CRIRES data.

### 3. Analysis

Both CO emission and absorption are detected from IRS 48 (Figure 2). CO emission is seen in the v=2-1 and very weak v=3-2 lines, while the isotopologues, C $^{18}$ O and C $^{17}$ O, are in absorption. The  $^{12}$ CO and  $^{13}$ CO v=1-0 lines contain a blend of the two components with absorption at the line center and emission at higher velocities. The absorption lines disappear at energy levels higher than P(6), indicating that the absorbing gas is cold with an excitation temperature of  $<30$  K. The emission lines are all well resolved spectrally with CRIRES and are double peaked, including more excited transitions free from absorption.

Weak CO ice absorption produces a broad shallow feature between 4.66 and 4.685  $\mu\text{m}$  and the HI Pf $\beta$  line is observed at 4.653  $\mu\text{m}$ , underlying the CO  $v=2-1$  R(8) line. The H<sub>2</sub>  $v=0$  S(9) line at 4.6947  $\mu\text{m}$  is not detected.

The CRİRES AO system produces a small enough PSF in the spatial direction that bright extended emission can be seen directly in the sky-subtracted 2-D images. The continuum was subtracted based on the mean continuum spatial profile and a scaled telluric standard was divided out at every spatial position. The IRS 48 emission lines are spatially extended in the 2-D spectra before extraction, particularly clearly in the observations taken at a position angle of 90°. Figure 3 shows the <sup>12</sup>CO extended emission in the continuum subtracted 2-D spectral trace.

Extended emission is unusual among the larger sample of mostly T Tauri stars studied with CRİRES, where most sources show no detectable extended emission in the 2-D images (Brown et al. 2011, in prep.). The lines are narrow with a width at line base of 18 km s<sup>-1</sup> while most of the parent sample show line widths well over 50 km s<sup>-1</sup> unless the disk is known to be face-on. The narrow width, and thus lack of high velocity gas, is consistent with gas motions from large radii and limits the inner extent of the gas, assuming Keplerian motion. Figure 4 shows the spatial cross section of the clean <sup>12</sup>CO stacked lines.

By extracting the spectra on a per spatial pixel basis, the physical location of the different components is probed (see Figure 5). The CO lines on the central stellar position appear in absorption in lines with  $J < 7$  and have little emission in all transitions. Strong <sup>12</sup>CO  $v=1-0$  and  $v=2-1$  emission lines can be seen at distances further from the star. Two components are visible: a redshifted component to the west and a blueshifted component to the east. The maximum flux is seen at  $\sim 30$  AU (6 pixels) from the central star. The spectra taken at a position angle of 0° show emission in both directions centered around 0 km s<sup>-1</sup> (Figure 5), in agreement with the 90° position angle of the ring seen in the 18.7  $\mu\text{m}$  dust image (Geers et al. 2007). There are, however, some asymmetries apparent in the PA=0° data with the north side being brighter and more strongly peaked towards the line center. A similar brightness asymmetry between the north and south sides of the ring is seen in the 18.7  $\mu\text{m}$  dust (Figure 5, Geers et al. 2007).

One additional calculation that can be made from the 2-D data is an inclination estimate based on the assumption of a symmetrical tilted disk. The major axis is determined to be 56 AU  $\pm$  2 AU peak to peak and 120 AU  $\pm$  5 AU in full extent. The minor axis is 42 AU  $\pm$  2 AU peak to peak and 80 AU  $\pm$  5 AU in full extent. Assuming a position angle of 90°, the inclination is then 42°  $\pm$  6°.

## 4. Velocity structure

### 4.1. Spectroastrometry

Spectroastrometry, determining the line flux spatial mean and standard deviation in every velocity bin, provides a convenient framework to model the emission in IRS 48 (e.g. Pontoppidan et al. 2008, 2011a). Collapsing the spatial information in this fashion provides several advantages. The biggest source of uncertainty in the direct imaging is almost certainly the continuum subtraction. Spectroastrometry, however, is ideally suited for recovery of weak contrast line signal from strong continuum. While this is less of a problem in the brightest flux spectral bins of the  $^{12}\text{CO}$  lines, the contrast in the line wings and weaker transitions of CO  $v=2-1$  and  $^{13}\text{CO}$  is significantly worse. The more limited information also makes modeling easier than full 2-D modeling while retaining the main characteristics of the spatial distribution.

The spectroastrometric signal is the flux-weighted center of the spectral trace. The weighted mean ( $\chi$ ) was found according to the formula  $\chi = \Sigma x_i F_i / \Sigma F_i$  where  $x_i$  is the spatial position and  $F_i$  is the flux at that point. The continuum has a dilution effect on the observed line signal. The signal that is actually measured has a contribution from both the continuum and the line so  $\chi_{Total}(\nu) F_{Total} = \chi_{Total}(\nu) (F_C + F_L) = \chi_C(\nu) F_C + \chi_L(\nu) F_L$ , where subscript  $C$  denotes the continuum component and subscript  $L$  represents the line component of both the flux ( $F$ ) and the weighted mean ( $\chi$ ). We assume that the continuum flux is pointlike and thus  $\chi_C = 0$ . The actual line spatial center is therefore  $\chi_L(\nu) (1 + F_C(\nu)/F_L(\nu))$ , where  $F_C/F_L$  is the continuum to line flux ratio. The  $^{12}\text{CO}$  lines in IRS 48 are relatively faint so  $F_C/F_L$  is  $\sim 9$  in the line center, resulting in significant dilution in the measured signal.  $F_C/F_L$  becomes increasingly large in the line wings as the signal becomes fainter.

To measure the width of the emitting region, we turn to the second moment or variance ( $\sigma^2$ ), representing the standard deviation ( $\sigma$ ) of the signal. It can be found using the formula  $\sigma^2 = \Sigma (x_i - P)^2 F_i / \Sigma F_i$  where  $x_i$  and  $F_i$  are as above.  $P$  is the central spatial position taken as the peak position of the continuum emission at  $4.7 \mu\text{m}$ . The variance is similarly continuum diluted such that  $\sigma_{Total}^2(\nu) F_{Total} = \sigma_{Total}^2(\nu) (F_C + F_L) = \sigma_C^2(\nu) F_C + \sigma_L^2(\nu) F_L$ . However, the continuum does have a standard deviation due to the telescope PSF and seeing so  $\sigma_C^2 \neq 0$ . Here,  $\sigma_L^2 = \sigma_{Total}^2(1 + F_C(\nu)/F_L(\nu)) - \sigma_C^2 F_C(\nu)/F_L(\nu)$ . A further correction to examine the line width around the line center, so  $P = \chi_L$ , can be made by subtracting  $\chi_L^2$  so  $\sigma_{L,P=\chi_L}^2 = \sigma_L^2 - \chi_L^2$ . The plots present  $\sigma_L$  which can then be compared with the PSF determined from the width of the continuum signal. Directly calculating the variance in the line center gives an emitting region width of  $4 \text{ AU }^{+10 \text{ AU}}_{-4 \text{ AU}}$  centered around the line center. However, this estimate is likely too large as each spectral pixel covers a range of radii due to

the curvature of the ring. A more detailed and accurate discussion of the line extent using simple models can be found in Section 4.2.

Figure 6 shows the detected fluxes, spatial centers and variances of the  $^{12}\text{CO}$ ,  $^{12}\text{CO}$   $v=2-1$  and  $^{13}\text{CO}$  emission lines. The spectroastrometric signals are calculated over 25 pixels (129 AU) which includes all the flux, with larger ranges only increasing the noise. Lines are stacked to enhance the signal. Only lines without line overlap and central absorption are included. For  $^{12}\text{CO}$ , this includes P(7), P(8) and P(11). For  $^{13}\text{CO}$ , it includes R(9), R(11), R(12) and R(13). CO  $v=2-1$  has the most clean lines as even the low energy rotational levels are free of absorption, including P(1), P(2), P(3), R(1), R(2), R(5), and R(6). The line shapes of all the isotopologues are similar but the absolute measured signals are different due to stronger continuum dilution in the weaker lines. Multiplying by the correction factors (2.8 for CO  $v=2-1$ /CO  $v=1-0$  and 4.6 for  $^{13}\text{CO}$ /CO  $v=1-0$ ), results in identical spectroastrometric signatures within the noise (Figure 6). All of the transitions are therefore emitting from the same physical region.

Figure 7 shows the spectroastrometric signatures arising from the different epochs. Observation in three different epochs 3-9 months apart allows us to search for variability. While the continuum width varied between the different nights due to AO performance, the CO structure appears stable over the year timescale.

## 4.2. Kinematic modeling

A simple Keplerian disk model is fitted to the data to examine the physical structure of the CO (following Pontoppidan et al. 2008). The model is gridded in the disk frame with rings of gas at the Keplerian velocity. Each ring is assigned a temperature according to an overall disk temperature profile. The surface density is assumed to be constant with a total column density,  $N_{\text{CO}}$ . The local line width is set to  $3 \text{ km s}^{-1}$ , the instrumental spectral resolution. The flux at each grid point is determined for the different rotational lines. The grid is then transformed into the observer’s Cartesian coordinates by twisting to the correct position angle and inclination. The emission is so extended that the  $0''.2$  slit does not capture all the light, so the data is corrected for the truncation accounting for the AO-corrected PSF of  $0''.18$  based on the measured continuum width (see Fig. 7). The emission in the  $\text{PA}=0^\circ$  position is strongly limited by this parameter.

A grid of models varying the stellar mass, inclination, inner radius ( $R_0$ ) and position angle were run to examine the interdependence of these parameters. The two most interesting parameters are the inner radius and the stellar mass. In order to robustly determine the



inner radius regardless of mass, the minimum  $\chi^2$  value for each mass was determined. Figure 9 plots mass against  $R_0$ , assuming the inclination associated with the minimum value. The hole size ( $R_0$ ) minimum is 30 AU throughout the mass range with optimal inclinations of  $50^\circ$  at the low mass end and  $30^\circ$  at the high mass end (Figure 9).

Stellar mass is degenerate with inclination in these models. Accurately determining the inclination is therefore the best method of determining the stellar mass. The inclination from Geers et al. (2007) is  $48^\circ \pm 8^\circ$ , which becomes incompatible with masses higher than  $3 M_\odot$ . The CRİRES 2D images give a slightly more face-on inclination measurement of  $42^\circ \pm 6^\circ$  (see §3). Figure 10 shows the  $\chi^2$  values for stellar mass versus inclination with the CRİRES inclination overlaid. The stellar mass of  $2 M_\odot \pm 0.5 M_\odot$  agrees with the determination from the optical spectra and is incompatible with a 1 Myr A0 star.

As the surface density is held constant, the temperature profile is also a proxy for the distribution of gas. We test two different distributions, a power-law and a uniform temperature ring. The power law distribution is of the form,  $T = T_0(R/R_0)^{-q}$ , where  $R_0$  is taken to be the inner most edge of the gas and the power-law declines from there until the outer edge of the disk, set at 100 AU.  $T_0$  is set at 260 K in agreement with the rotation diagram results from section 5.1. A steep power law index ( $q > 0.4$  for best results) is required in order to show the double peaked flux profile. The uniform temperature ring is centered at  $R_0$  and  $T_0$  but has width  $\Delta R$ . The effects of varying emission widths in a uniform temperature ring with constant density are shown in Figure 9. The width of the emitting region is directly related to the variance,  $\sigma_L^2$ . The best fits result from the narrowest emitting regions, limited only by the grid cell size. Overall there was little difference between the two distributions as the good fits from both concentrated the emission close to  $R_0$  with a width of a few AU or less. Physically this narrow region is likely the dust hole cavity wall.

In summary, the best fit to the data was obtained using the derived stellar mass of  $2 M_\odot$  (§2.2) and an inclination of  $42^\circ$  from the 2-D CRİRES data (Figure 8). The hole size is 30 AU with the disk at a position angle of  $95^\circ$ , in good agreement with the mid-IR image. The model fit of the PA= $0^\circ$  observations is not as good due to the asymmetries in the data (i.e. Figure 5). The structure appears more complex than a simple uniform ring in that direction.

## 5. Excitation

### 5.1. Rotational temperatures

Rotation diagrams, which use the relative strengths of the rotation lines to understand the gas temperature and column density, were constructed for both the emission and absorption components. Interpretation of rotation diagrams is commonly based on the Boltzmann distribution and the assumption of LTE level populations, so

$$\frac{n_J}{g_J} = \frac{n_{CO}}{Q_{Rot}} e^{(E_J/kT)}, \quad (1)$$

where  $n$  is the number,  $Q_{Rot}$  is the partition function, and  $E_J$  is the energy of level  $J$ . We plot  $\ln(F_J/gA\nu)$  against  $E_{Upper}/k$  where  $F_J$  is the line flux,  $g$  is the degeneracy ( $2J_{Up}+1$ ),  $A$  is the Einstein A coefficient,  $\tilde{\nu}$  is wavenumber in  $\text{cm}^{-1}$  and  $E_{Upper}$  is the upper state energy. In the optically thin case, a linear fit will match the data well. The slope ( $\alpha$ ) is related to the temperature,  $T_{Rot}$  such that  $T_{Rot} = -1/\alpha$ . The intercept,  $y$ , is related to the CO column density,  $N_{CO}$ , such that

$$N_{CO} = Q_{Rot} e^y \frac{16\pi d^2}{hc A_{emit}} \quad (2)$$

where  $d$  is the distance and  $A_{emit}$  is emitting area.

#### 5.1.1. Absorption lines

The absorption lines are strongest in the lowest energy rotational lines and absorption features can be seen in the less abundant isotopes,  $^{13}\text{CO}$ ,  $\text{C}^{18}\text{O}$  and  $\text{C}^{17}\text{O}$ . The absorption lines are spectrally unresolved at  $3 \text{ km s}^{-1}$  and have a central  $v_{\text{LSR}}$  of  $3.8 \text{ km s}^{-1}$  in agreement with the  $\rho$  Ophiuchi region (e.g. Di Francesco et al. 2004; Maruta et al. 2010). The derived gas excitation temperatures from the different isotopologues are  $\sim 25 \text{ K}$  (see bottom half of Table 3). The  $^{12}\text{CO}$  absorption is also highly optically thick. These cold temperatures are consistent with an origin in foreground cloud material. The absorption lines are therefore probably not related to the disk and are excluded from further analysis.

#### 5.1.2. Emission lines

Quantifying the emission line fluxes is complicated by the contaminating absorption lines at low  $J$ . A clean template of the emission line profile is made by stacking the higher  $J$  lines which are free from absorption. This template proves to be a good match for the

CO  $v=2-1$  and  $^{13}\text{CO}$  emission lines as well as the CO  $v=1-0$ . The profile is then fitted via chi-squared minimization on top of a measured local continuum to derive each line flux. This method provides more consistent measurements than integrating the flux directly which is strongly affected by noise. The low  $J$   $^{12}\text{CO}$  lines are contaminated at low velocities by absorption, so a fit was made to the line wings.

The rotation diagram (Figure 11) for  $^{12}\text{CO } v=1-0$ ,  $^{12}\text{CO } v=2-1$  and  $^{13}\text{CO}$  relative to the energy of  $J=0$  in each vibrational level indicates that the different transitions have similar properties. The distributions all appear linear, in agreement with optically thin gas at a single temperature. In this case, the derived rotation temperatures are  $\sim 250$  K (Table 3). Small changes in the derived slope (i.e. temperature) can result in large changes in derived population. All the slopes are in the range 100-260 K, but the better constrained species are at the higher end. The total mass ( $N_{\text{CO}} \times A_{\text{emit}}$ ) is well constrained, but the column density is not due to the lack of constraints on the emitting area. Based on the kinematics (§4.2), we estimate that the area is a ring at 30 AU with a width of 0.5 AU and use this area to calculate the column densities in Table 3. A gas temperature of 250 K is slightly high compared to the likely dust temperature of  $\sim 150$  K at 30 AU based on the low luminosity of the star. However, the gas temperature may be much higher than the dust temperature due to strong UV radiation. The CO  $v=2-1$  lines are too strong to be purely thermally excited with a vibrational temperature much higher than the rotational temperature. We attribute the excess excitation to UV fluorescent excitation which is discussed in Section 5.2. The low CO  $v=1-0$  lines may be slightly optically thick but the errors are large due to the central absorption lines and a linear fit is well within the errors. However, the optically thin fits produce a low isotopic ratio  $^{12}\text{CO}/^{13}\text{CO}$  of 15, challenging this assumption.

In order to determine a limit on the amount of CO within the hole, flux limits were determined from the 2-D images. In general, the flux levels were similar to residuals from the continuum subtraction in regions without CO emission and were on the order of 10% of the peak flux. Assuming optically thin gas, rotation diagrams for gas at different temperatures were compared with the flux limits to determine the maximum CO gas mass that could be within the hole without detection (Figure 12). The amount is strongly dependent on temperature with much lower limits at high temperatures and weaker constraints at low temperatures. In general, the inner region should be hotter than the gas further out. The mass limit is  $\sim 10^{20}$  g for temperatures above 500 K. This translates to a gas density of  $\sim 10^3 \text{ cm}^{-3}$ , assuming a uniform distribution within the 30 AU hole and a disk height resulting from hydrostatic equilibrium.

## 5.2. UV fluorescent excitation

The distance of the gas from the star, resulting in cooler temperatures, and the presence of high energy CO  $v=2-1$  and  $v=3-2$  lines suggest that a non-equilibrium process such as UV fluorescence is likely responsible for their line emission. The measured vibrational temperature is 2200 K, greatly in excess of the thermal rotational temperature of 260 K. A strong UV field is to be expected from an A type star such as IRS 48 and the strong PAH emission from within the hole requires its presence.

A simple UV fluorescence model was run to examine the likelihood of the stellar UV field producing the observed vibrationally excited emission at 30 AU. The model follows Brittain et al. (2007) but expands the vibrational levels covered to 35  $X^1\Sigma^+$  and 25  $A^1\Pi$  levels. The model assumes statistical equilibrium so each level maintains a steady population. We then considered excitation from  $X^1\Sigma^+$  to  $A^1\Pi$  ( $g_{A-X}$ ) balanced by spontaneous emission ( $A_{A-X}$ ) back to the ground electronic state. Decay out of the excited electronic state populates a range of vibrational levels in the ground state, including vibrational levels which are too energetic to be thermally populated. We also include spontaneous relaxation between vibrational levels in the ground electronic state ( $A_{X-X}$ ), which occurs primarily between levels with  $\Delta v = 1$ . The transitions covered between the ground state  $X^1\Sigma^+$  electronic state and the  $A^1\Pi$  excited electronic state occur at ultraviolet wavelengths 1270 to 4000 Å, but the most populous levels are mainly driven in the range 1270 to 1700 Å. The model also includes collisional excitation, assumed to be thermalized at  $T_0 = 260$  K.

In general, the model output depends purely on the input UV spectrum. While accretion shocks produce much of the UV emission in lower mass T Tauri stars, the similarity between the photospheric and shock temperatures in Herbig Ae stars results in the photospheric emission dominating (Valenti et al. 2000). Based on our derived stellar properties, we constructed a 9000 K blackbody and compared this to an HST STIS UV spectrum of AB Aur (from StarCAT<sup>2</sup>). AB Aur is a good proxy for IRS 48 with a spectral type of A0 and age of 4 Myr. While the spectrum contains many lines, the overall flux and shape is a good match to the 9000 K blackbody, once scaled to the appropriate luminosity. The calculations used the observed spectrum in the available range (1140-1729 Å), which accounts for 99% of the transitions in this source, and the blackbody at longer wavelengths.

The observed fractional population in each vibrational level was calculated using the rotational diagrams (Figure 11). The energies of each rotational state were normalized to the zero point of each vibrational level. The intercept was used to derive the population in

---

<sup>2</sup><http://casa.colorado.edu/~ayres/StarCAT/>

each level, which was then divided by the total population. The ground state  $v=0$  is by far the most populated. The low signal-to-noise in many of the faint lines introduces a lot of scatter in the rotational diagram. Given the similarity in line profiles and spectroastrometry, the gas is likely all close in temperature so we fix the rotational temperatures at 260 K and then derive the populations.

Figure 13 shows the vibrational diagram with the overlaid model fit. A linear fit to the data ( $v > 0$ ) gives a vibration temperature of 2200 K, significantly higher than the rotational temperature. However, the thermal component to the  $v'=1$  level is significant, actually causing the vibrational temperature to be underestimated. The model of the effect of the UV field at 30 AU, including the thermal contribution from gas at 260 K under the assumption of LTE excitation, is shown in red while the purely vibrational excitation is shown in blue. For  $v=2$  and 3, the blue points lie completely under the red as there is virtually no collisional excitation to these levels. The vibrational temperature of the model is  $\sim 5000$  K. The model fit is in excellent agreement with the data, indicating that the expected UV field from IRS 48 for  $M_* = 2 M_\odot$  and  $L_* = 14.3 L_\odot$  can produce the observed energy distribution.

We also investigate the expected excitation from the younger, higher mass star implied by the evolutionary age of  $\rho$  Oph (§2.2). The luminosity is set at  $200 L_\odot$  and the distance is kept at the 120 pc distance to  $\rho$  Oph. The black crosses in Figure 13 represent the expected excitation from such a star at 30 AU. While the vibrationally excited emission increases by about an order of magnitude, the collisional excitation also increases due to a higher temperature of 500 K at 30 AU. It appears unlikely that IRS 48 is a younger, more luminous, but highly extincted star. One remaining potential source of error in the luminosity would be an incorrect distance, implying that IRS 48 is not actually in the  $\rho$  Oph molecular cloud. The vibrational excitation does not provide a constraint on this scenario as a larger distance simply corresponds to a large hole size and the vibrational diagram is unchanged.

## 6. Discussion

Based on our CRIRES data, the CO emission around IRS 48 comes from a ring at 30 AU in Keplerian rotation around the central star. We propose that the CO gas is thermally and UV excited in the dust wall at the hole edge. The radius of the gas emission and the dust hole edge seen in the Geers et al. (2007)  $18.7 \mu\text{m}$  dust image are similar, indicating that the CO and dust rim are co-spatial. Our Keplerian model is consistent with a ring of emission with little to no flux required from outside the hole wall region, as seen in the required steep

power law index. The majority of the stellar UV light must reach the hole wall in order to excite the CO  $v=2-1$  and  $v=3-2$  emission seen along with the  $v=1-0$  emission, given the good match between the fluorescence model and data. While little dust shielding is likely present inside the hole, the PAH molecules could absorb some of the UV field. Although without knowing either the abundance or distribution of the PAHs, it is difficult to estimate the magnitude of the absorption. The hole wall may be vertically puffed up so that a fraction of the stellar UV light reaches the rim unattenuated.

Despite the lack of CO interior to 30 AU, some material is present in the inner disk. The strong, centrally-peaked PAH emission seen by Geers et al. (2007) indicates that small particles remain within the dust hole in IRS 48. Generally, PAHs are small enough that they are expected to be dynamically coupled to the gas. The presence of PAHs also promotes the formation of  $H_2$ , CO and other small molecules even in the absence of small grains (Jonkheid et al. 2006). Other signs of material inside the hole are the  $H\alpha$  lines in both our 2008 and the Geers et al. (2007) optical spectra and the  $Pf\beta$  line present in all the CRIRES data - all probable signs of ongoing accretion. We know little about the distribution of gas within the hole from these signatures although material is likely still reaching the star.

Any overall picture of the IRS 48 system must therefore explain both the truncation of the dust grains and CO at 30 AU as well as the destruction of CO, but not PAHs and atomic hydrogen, within the hole. The strong UV field within the hole may be the cause of the different survival rates. Larger PAH molecules have a better chance of surviving in high UV environments than smaller ones. According to Visser et al. (2007), PAHs of sizes 50 carbon atoms and smaller are destroyed at the  $\tau=1$  surface out to 100 AU around a Herbig Ae/Be star. Given the likely low opacity of the disk interior only PAHs with 100 carbon atoms or greater would be able to populate the hole outside of about 5 AU, sufficient to explain the mid-IR VISIR images. On the other hand, CO has a photodissociation lifetime of  $< 1$  year inside the hole without shielding. Preliminary modeling indicates that gas densities below  $10^5 \text{ cm}^{-3}$  are inadequate for rapid reformation of CO and prevent self-shielding (Bruderer, priv. comm.). Our limits on the CO gas density within the hole lie well below this value for temperatures greater than 500 K. However, the CRIRES data can give little constraint on any low temperature gas. Gas with temperatures of 300 K or less could be present at densities of  $10^5 \text{ cm}^{-3}$ . This regime of PAH emission but no CO emission places stringent limits on the amount of gas present in the hole.

The sharp truncation of CO and dust points towards either physical truncation by a companion or photoevaporation of the CO. While the UV field around IRS 48 is strong and the accretion signatures are weak, it is not clear that photoevaporative inside-out clearing would leave the material inside the hole in this state (e.g. Alexander et al. 2006, Owen et al.

2011). Gas and dust inside the hole in the photoevaporative clearing scenario is usually residual material still draining onto the star and is not being replenished. This system would thus have to be in a specific time period where the gap has open, the density of the interior material has dropped below the CO photodissociation threshold but has not yet drained completely. A companion, on the other hand, would naturally reduce the flow of material inwards and create a drop in density of both gas and dust. A final possibility, although probably the least likely, is that no material is flowing through the hole and the PAHs are formed in situ via the collision of large rocky bodies.

The CO hole in the Oph IRS 48 disk is the largest gas ring discovered to date for any pre-main sequence star. The hole is more than twice as large as the 11 AU holes around the Herbig Ae/Be stars, HD 141569 and HD 97084, which have similar spectral types to IRS 48. SR 21, a G-type star, with a ring of emission at 7 AU is the lowest mass source with a known large near-IR CO hole (Pontoppidan et al. 2008). Vibrational emission of similar extent to the  $v=1-0$  lines in all cases indicates that the UV field may be the driving force in maintaining the presence of the CO holes via photodissociation. Large near-IR CO holes of  $>1$  AU have not yet been found in K- or M-type T Tauri transition disks, despite the presence of substantial dust holes. In fact, many transition disks contain CO close to the star at radii significantly smaller than the dust hole size (Pontoppidan et al. 2008; Salyk et al. 2011). The UV energy from T Tauri stars is significantly smaller than from higher mass stars with a large portion generated in accretion shocks. If transition disks have even smaller accretion rates than classical T Tauri stars as has been suggested (Najita et al. 2007), T Tauri stars are unlikely to have both an absence of absorbing inner dust and a strong UV field, hampering the creation of large photodissociated CO holes. Although CO fundamental emission is detected from the inner dust wall of IRS 48, any non-detection of CO emission from T Tauri disks with holes (e.g. CoKu Tau/4) may be caused by difficulty exciting the  $4.7 \mu\text{m}$  CO lines at large radii due to both the weaker UV field and lower temperatures, rather than a lack of gas at the inner rim of the dust disk. Further work to better understand the excitation of gas in holes is needed to determine if the creation of such large CO holes is a unique phenomenon of intermediate mass stars.

We are also left with an evolutionary puzzle regarding IRS 48. The CRIREs data, both from kinematics and excitation, are much more consistent with a lower mass star of around  $2 M_{\odot}$  and a luminosity of  $\sim 15 L_{\odot}$ , as derived from the optical spectroscopy. The data are inconsistent with a prototypical 1 Myr A0 star with a mass of  $4.5 M_{\odot}$  and luminosity of  $200 L_{\odot}$ . However, the resulting age from evolutionary tracks of  $\sim 15$  Myr is much older than the  $\sim 1$  Myr age of Ophiuchus (Luhman & Rieke 1999), with the star being underluminous by more than an order of magnitude. Such an old PMS star might be expected to have a debris disk of reprocessed dust and no gas, but this is clearly not the case for IRS 48. IRS 48 appears

to be a member of Ophiuchus with proper motions in agreement with the cloud (E. Mamajek, priv. comm.), a position close to the core, emission lines centered at the cloud velocity and an extinction consistent with a location within or behind the cloud. Baraffe et al. (2009) suggest that episodic cold accretion leads to different contraction timescales, and thus some stars may appear much older from evolutionary models than their true age. While IRS 48 is more massive than the stars studied by Baraffe et al. (2009), similar mechanisms may apply even at higher mass and help explain the apparent age discrepancy for IRS 48. If the stellar parameters, cloud membership and PMS evolutionary tracks are all correct, Oph IRS 48 would be an extremely old member of Ophiuchus, possibly left over from a previous epoch of star formation.

## 7. Conclusions

We have used the combination of high spatial and spectral resolution of CRIRES to observe spatially extended CO emission from Oph IRS 48. IRS 48 was known to be a transitional disk from the imaged  $18\ \mu\text{m}$  dust ring but the centrally peaked PAHs lead to an expectation of interior gas (Geers et al. 2007). Despite the presence of PAHs within the dust hole, the CO emission peaks at 30 AU, co-spatial with the dust hole edge, and shows no emission interior to the dust hole. The spatial distribution of the vibrationally excited gas and isotopologues is the same, indicating a common origin. The CO geometry is in agreement with the Geers et al. (2007) dust image with an east-west major axis, brighter emission from the north side compared to the south, and a derived inclination of  $42^\circ \pm 6^\circ$ . The gas is thermally excited to a temperature of 260 K, but is also strongly fluoresced by the central star’s UV field, showing vibrational excitation temperatures of  $\sim 5000$  K. The new spectral type of  $A0_{-4}^{+0}$  resolves the discrepancy of strong PAHs around what was thought to be an M0 star (Geers et al. 2007) and explains the vibrationally excited emission. Our kinematic modeling is consistent, both spectrally and spatially, with a ring of gas at 30 AU in Keplerian rotation with a width of only a few AU or less. All the evidence points towards the gas being UV excited in the outer rim of the hole. A sudden drop in density to  $<10^5\ \text{cm}^{-3}$ , as might be caused by a companion, could cause the CO to photodissociate on short timescales but maintain the larger PAH population. IRS 48 is therefore an excellent target for planet finding follow-up.

The authors wish to thank Vincent Geers for providing the reduced data from his 2007 paper and Eric Mamajek for discussion of the cloud membership of IRS 48. J.M. Brown acknowledges the Smithsonian Astrophysical Observatory for support from a SMA fellowship. Astrochemistry at Leiden is supported by a Spinoza grant from the Netherlands



Organization for Scientific Research (NWO) and by the Netherlands Research School for Astronomy (NOVA) grants.

## REFERENCES

- Acke, B., Min, M., van den Ancker, M. E., Bouwman, J., Ochsendorf, B., Juhasz, A., & Waters, L. B. F. M. 2009, *A&A*, 502, L17
- Alexander, R. D. & Armitage, P. J. 2009, *ApJ*, 704, 989
- Alexander, R. D., Clarke, C. J., & Pringle, J. E. 2006, *MNRAS*, 369, 229
- Andrews, S. M., Wilner, D. J., Espaillat, C., Hughes, A. M., Dullemond, C. P., McClure, M. K., Qi, C., & Brown, J. M. 2011, *ApJ*, 732, 42
- Artymowicz, P. & Lubow, S. H. 1994, *ApJ*, 421, 651
- . 1996, *ApJ*, 467, L77+
- Baraffe, I., Chabrier, G., & Gallardo, J. 2009, *ApJ*, 702, L27
- Blake, G. A. & Boogert, A. C. A. 2004, *ApJ*, 606, L73
- Brittain, S. D., Najita, J. R., & Carr, J. S. 2009, *ApJ*, 702, 85
- Brittain, S. D., Simon, T., Najita, J. R., & Rettig, T. W. 2007, *ApJ*, 659, 685
- Brown, J. M., Blake, G. A., Dullemond, C. P., Merín, B., Augereau, J. C., Boogert, A. C. A., Evans, II, N. J., Geers, V. C., Lahuis, F., Kessler-Silacci, J. E., Pontoppidan, K. M., & van Dishoeck, E. F. 2007, *ApJ*, 664, L107
- Brown, J. M., Blake, G. A., Qi, C., Dullemond, C. P., Wilner, D. J., & Williams, J. P. 2009, *ApJ*, 704, 496
- Brown, J. M., Pontoppidan, K. M., van Dishoeck, E. F., Herczeg, G. J., et al. 2011, *A&A*, in prep.
- Bryden, G., Chen, X., Lin, D. N. C., Nelson, R. P., & Papaloizou, J. C. B. 1999, *ApJ*, 514, 344
- Calvet, N., D’Alessio, P., Hartmann, L., Wilner, D., Walsh, A., & Sitko, M. 2002, *ApJ*, 568, 1008

- Crida, A. & Morbidelli, A. 2007, MNRAS, 377, 1324
- Di Francesco, J., André, P., & Myers, P. C. 2004, ApJ, 617, 425
- Dullemond, C. P. & Dominik, C. 2004, A&A, 417, 159
- Geers, V. C., Pontoppidan, K. M., van Dishoeck, E. F., Dullemond, C. P., Augereau, J.-C., Merín, B., Oliveira, I., & Pel, J. W. 2007, A&A, 469, L35
- Goto, M., Usuda, T., Dullemond, C. P., Henning, T., Linz, H., Stecklum, B., & Suto, H. 2006, ApJ, 652, 758
- Hillenbrand, L. A., Strom, S. E., Vrba, F. J., & Keene, J. 1992, ApJ, 397, 613
- Huélamo, N., Lacour, S., Tuthill, P., Ireland, M., Kraus, A., & Chauvin, G. 2011, A&A, 528, L7+
- Indebetouw, R., Mathis, J. S., Babler, B. L., Meade, M. R., Watson, C., Whitney, B. A., Wolff, M. J., Wolfire, M. G., Cohen, M., Bania, T. M., Benjamin, R. A., Clemens, D. P., Dickey, J. M., Jackson, J. M., Kobulnicky, H. A., Marston, A. P., Mercer, E. P., Stauffer, J. R., Stolovy, S. R., & Churchwell, E. 2005, ApJ, 619, 931
- Jonkheid, B., Kamp, I., Augereau, J.-C., & van Dishoeck, E. F. 2006, A&A, 453, 163
- Kaeuff, H.-U., Ballester, P., Biereichel, P., Delabre, B., Donaldson, R., Dorn, R., Fedrigo, E., Finger, G., Fischer, G., Franza, F., Gojak, D., Huster, G., Jung, Y., Lizon, J.-L., Mehrgan, L., Meyer, M., Moorwood, A., Pirard, J.-F., Paufigue, J., Pozna, E., Siebenmorgen, R., Silber, A., Stegmeier, J., & Wegerer, S. 2004, in Proceedings of the SPIE, ed. A. F. M. Moorwood & M. Iye, Vol. 5492, 1218–1227
- Loinard, L., Torres, R. M., Mioduszewski, A. J., & Rodríguez, L. F. 2008, ApJ, 675, L29
- Luhman, K. L. & Rieke, G. H. 1999, ApJ, 525, 440
- Marois, C., Macintosh, B., Barman, T., Zuckerman, B., Song, I., Patience, J., Lafrenière, D., & Doyon, R. 2008, Science, 322, 1348
- Maruta, H., Nakamura, F., Nishi, R., Ikeda, N., & Kitamura, Y. 2010, ApJ, 714, 680
- Meeus, G., Waters, L. B. F. M., Bouwman, J., van den Ancker, M. E., Waelkens, C., & Malfait, K. 2001, A&A, 365, 476
- Meijer, J., Dominik, C., de Koter, A., Dullemond, C. P., van Boekel, R., & Waters, L. B. F. M. 2008, A&A, 492, 451

- Muzerolle, J., D'Alessio, P., Calvet, N., & Hartmann, L. 2004, *ApJ*, 617, 406
- Najita, J., Carr, J. S., & Mathieu, R. D. 2003, *ApJ*, 589, 931
- Najita, J. R., Strom, S. E., & Muzerolle, J. 2007, *MNRAS*, 378, 369
- Oke, J. B., Cohen, J. G., Carr, M., Cromer, J., Dingizian, A., Harris, F. H., Labrecque, S., Lucinio, R., Schaal, W., Epps, H., & Miller, J. 1995, *PASP*, 107, 375
- Owen, J. E., Ercolano, B., & Clarke, C. J. 2011, *MNRAS*, 412, 13
- Pickles, A. J. 1998, *PASP*, 110, 863
- Pontoppidan, K. M., Blake, G. A., & Smette, A. 2011a, *ApJ*, 733, 84
- Pontoppidan, K. M., Blake, G. A., van Dishoeck, E. F., Smette, A., Ireland, M. J., & Brown, J. 2008, *ApJ*, 684, 1323
- Pontoppidan, K. M., van Dishoeck, E., Blake, G. A., Smith, R., Brown, J., Herczeg, G. J., Bast, J., Mandell, A., Smette, A., Thi, W.-F., Young, E. D., Morris, M. R., Dent, W., & Käufl, H. U. 2011b, *The Messenger*, 143, 32
- Salyk, C., Blake, G. A., Boogert, A. C. A., & Brown, J. M. 2009, *ApJ*, 699, 330
- . 2011, *ApJ*, in press
- Siess, L., Dufour, E., & Forestini, M. 2000, *A&A*, 358, 593
- Skrutskie, M. F., Cutri, R. M., Stiening, R., Weinberg, M. D., Schneider, S., Carpenter, J. M., Beichman, C., Capps, R., Chester, T., Elias, J., Huchra, J., Liebert, J., Lonsdale, C., Monet, D. G., Price, S., Seitzer, P., Jarrett, T., Kirkpatrick, J. D., Gizis, J. E., Howard, E., Evans, T., Fowler, J., Fullmer, L., Hurt, R., Light, R., Kopan, E. L., Marsh, K. A., McCallon, H. L., Tam, R., Van Dyk, S., & Wheelock, S. 2006, *AJ*, 131, 1163
- Strom, K. M., Strom, S. E., Edwards, S., Cabrit, S., & Skrutskie, M. F. 1989, *AJ*, 97, 1451
- Valenti, J. A., Johns-Krull, C. M., & Linsky, J. L. 2000, *ApJS*, 129, 399
- van der Plas, G., van den Ancker, M. E., Acke, B., Carmona, A., Dominik, C., Fedele, D., & Waters, L. B. F. M. 2009, *A&A*, 500, 1137
- Visser, R., Geers, V. C., Dullemond, C. P., Augereau, J., Pontoppidan, K. M., & van Dishoeck, E. F. 2007, *A&A*, 466, 229

Weingartner, J. C. & Draine, B. T. 2001, ApJ, 548, 296

Zhu, Z., Nelson, R. P., Hartmann, L., Espaillat, C., & Calvet, N. 2011, ApJ, 729, 47

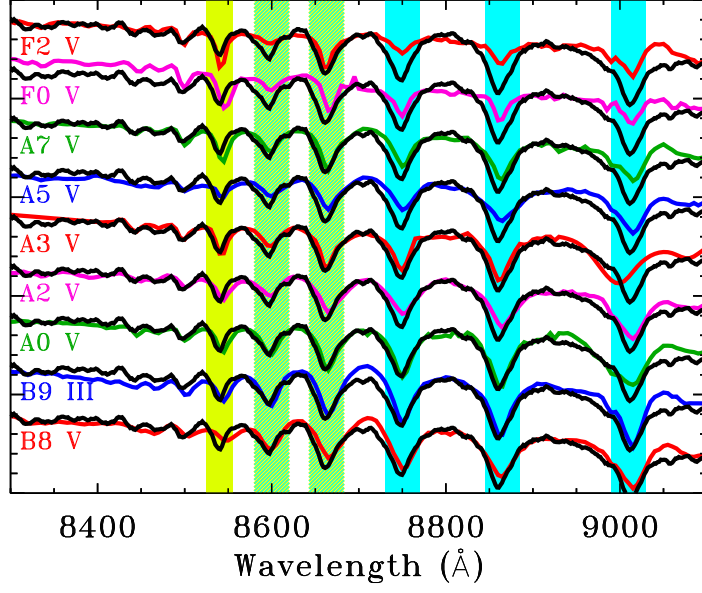


Fig. 1.— Comparison of the H Paschen series in the IRS 48 LRIS-ADC spectrum (black) with the Pickles (1998) spectral library. The presence and strength of these lines clearly indicates that IRS 48 is an A-type star, with a best fit of  $A0_{-1}^{+4}$ .

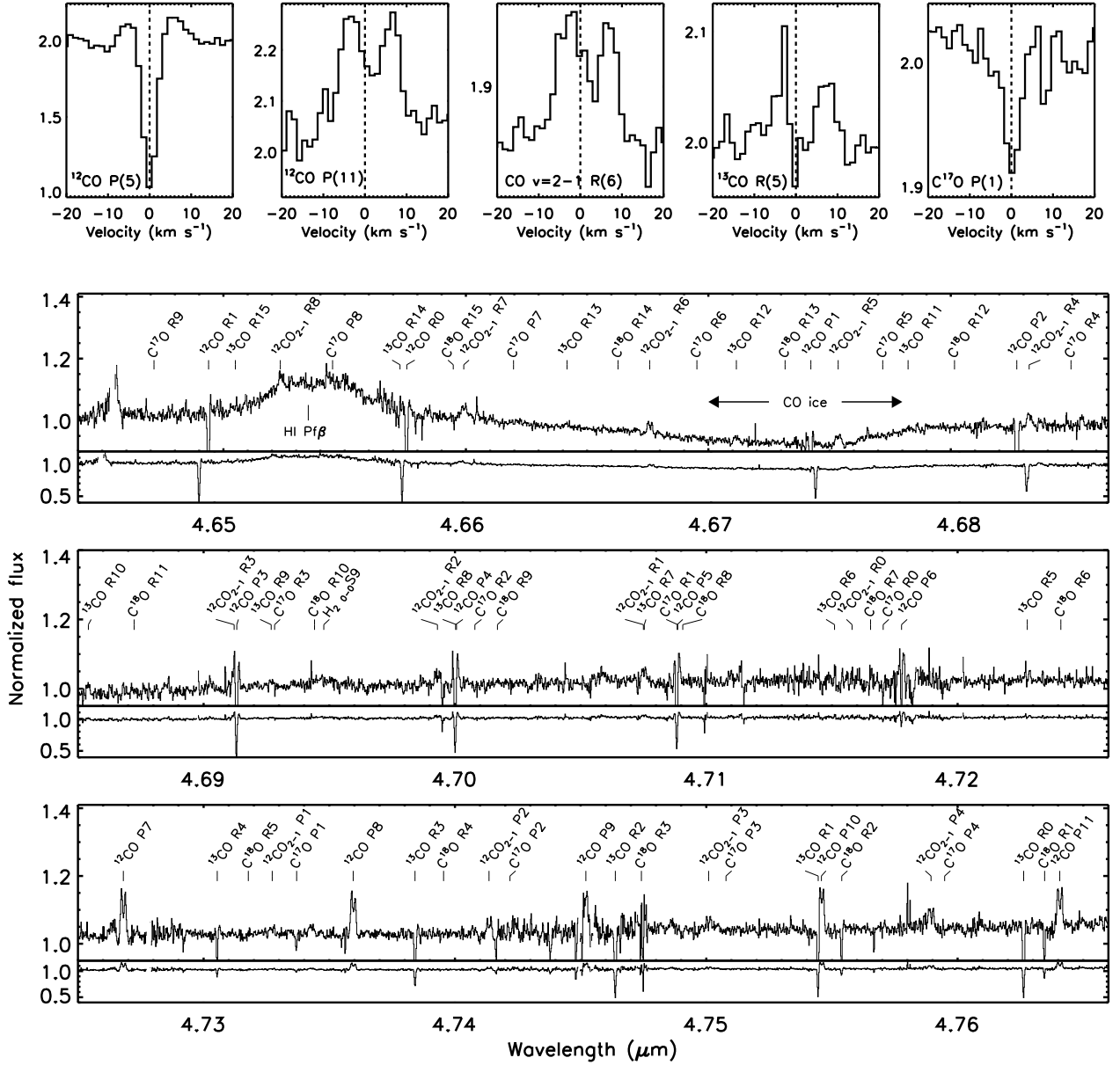


Fig. 2.— VLT-CRIRES spectrum of IRS 48 with the upper row showing close ups of different lines and the lower panels showing the emission lines in detail on the top and the full depth of the absorption lines on the bottom.  $^{12}\text{CO}$ ,  $^{13}\text{CO}$  and  $\text{C}^{18}\text{O}$  are seen in absorption, particularly strong in low energy  $J$  transitions. The  $^{12}\text{CO}$   $v=1-0$  and  $v=2-1$  lines show strong double peaked emission features.

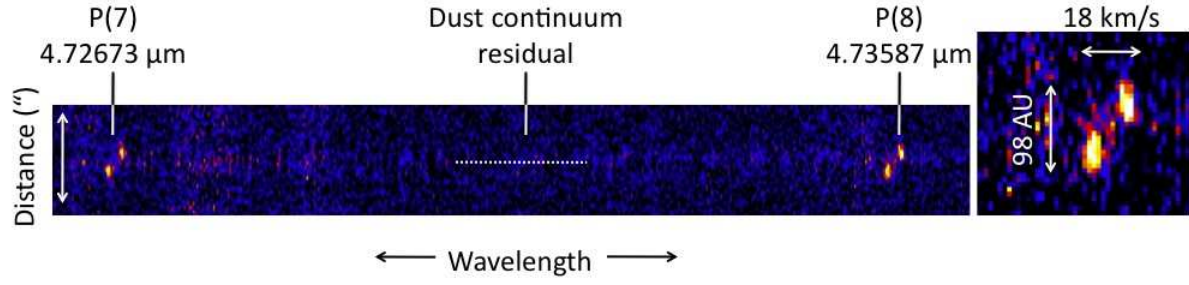


Fig. 3.— Continuum subtracted 2D spectra showing the extended line emission in the  $^{12}\text{CO}$  P(7) and P(8) lines from 2007 September 5. The emission peaks around 30 AU and is much weaker towards the central position.

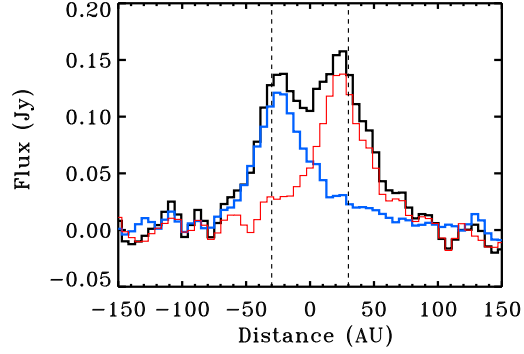


Fig. 4.— Cross section of the stacked lines at  $\text{PA}=90^\circ$ . The black line is the total spatial distribution while the blue and the red lines are the blue and red sides of the line. The peak emission averaged over the entire line width occurs at  $\pm \sim 25$  AU. This is slightly smaller than the largest peak to peak extents, marked with dashed vertical lines, due to the inclusion of gas not at apoapsis of the inclined ring. When compared directly to the continuum distribution, the CO spatial profiles are consistent with a small emitting region (see also §4.2).



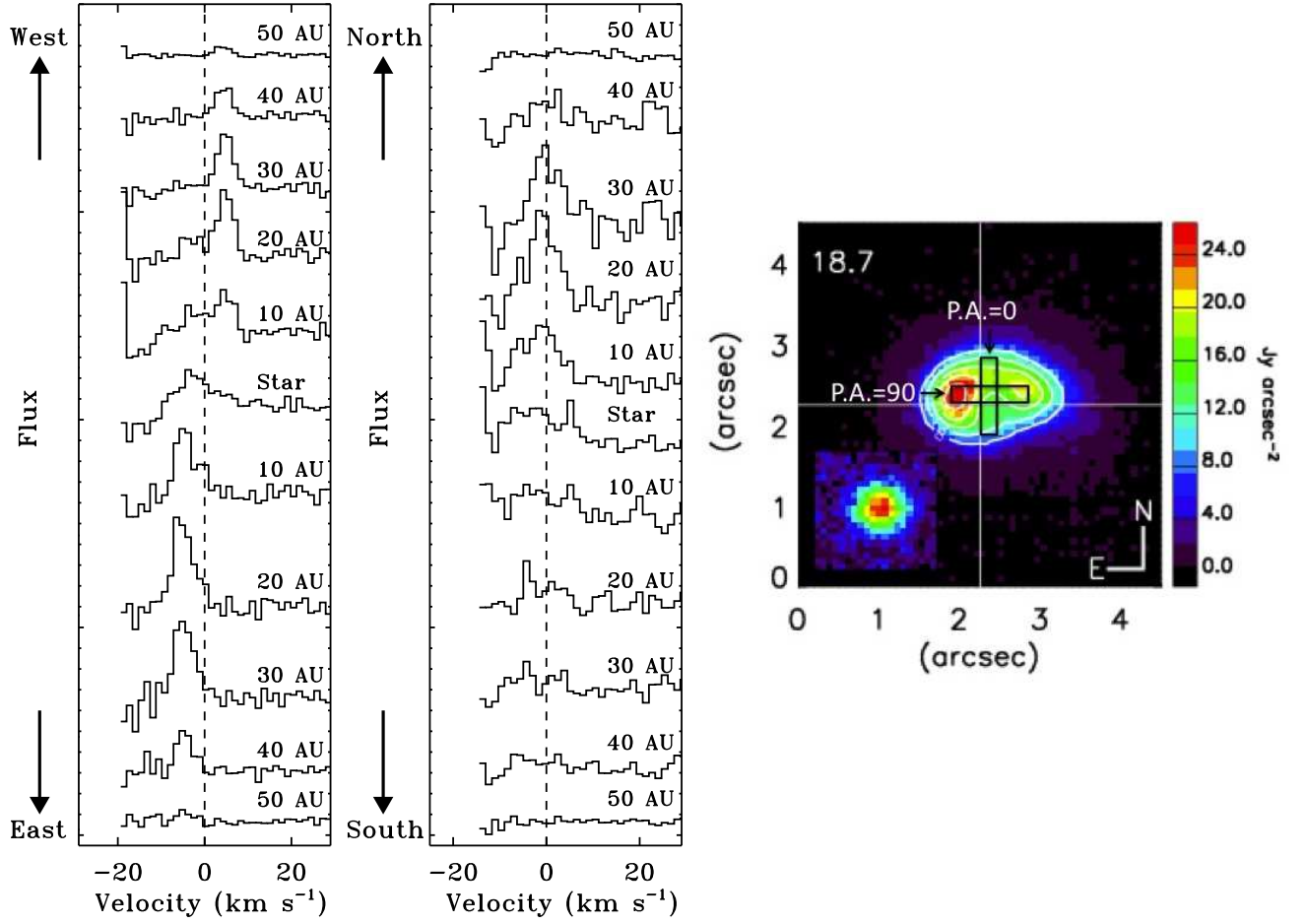


Fig. 5.— (Left) Spatial changes in the profile of the P(8) transition of  $^{12}\text{CO}$   $v=1-0$  in increments of 86 mas (10 AU) for PA=90° (left) and PA=0° (right). Emission occurs from the outer regions while line of sight absorption occurs towards the central star at lower  $J$  ( $<6$ ). Keplerian rotation can clearly be seen in the emission with the emission peak in the top spectra redshifted compared to the bottom. The missing data on the left, removed due to contamination by the telluric P(8) line, show the clear separation between science and sky lines. (Right) The slit positions overlaid on the Geers et al. (2007) 18.7  $\mu\text{m}$  image. Some of the asymmetries of the dust are echoed in the gas, including brighter emission in the eastern peak compared to the west and brighter emission from the north compared to the south.

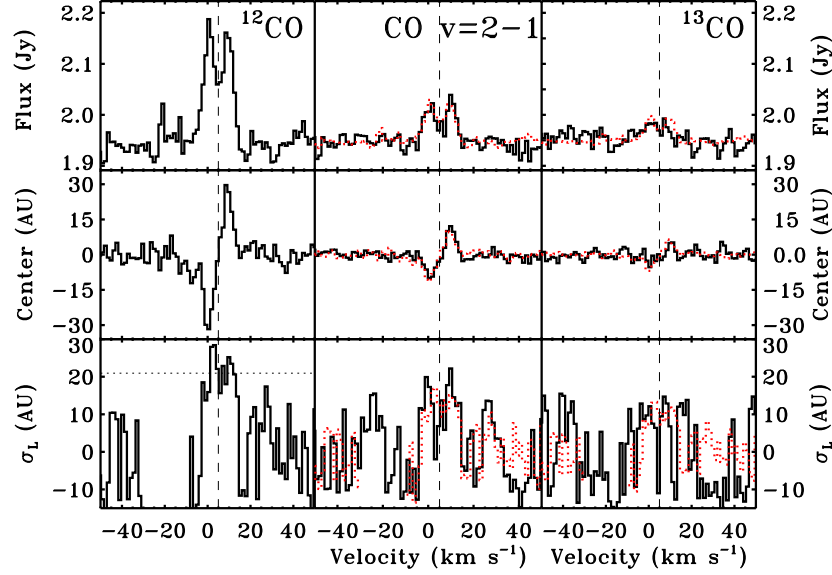


Fig. 6.— Comparison of the flux (top), spatial center (middle) and extent (bottom) of the IRS 48 CO lines for  $^{12}\text{CO}$  (left), CO  $v=2-1$  (middle), and  $^{13}\text{CO}$  (right) at a position angle of  $90^\circ$ . The  $v=1-0$  lines have been scaled to the appropriate flux ratio and overplotted as dotted red lines in the  $v=2-1$  and  $^{13}\text{CO}$  panels. The bottom panel shows the standard deviation of the line emission. The standard deviation of the continuum signal is shown as a dotted horizontal line in the  $^{12}\text{CO}$  panel. Deconvolving the PSF results in an emitting region width of  $4 \text{ AU}^{+10\text{AU}}_{-4\text{AU}}$ . The agreement in spatial position and line shape of the different transitions indicates that this emission comes from the same physical region.

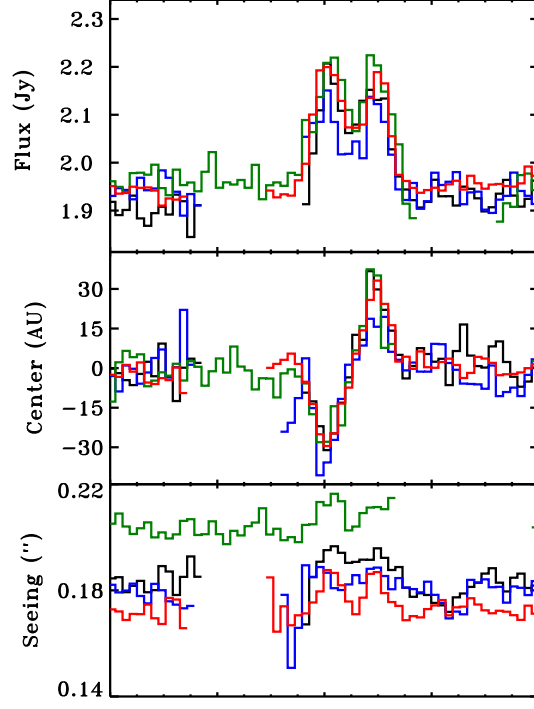


Fig. 7.— Comparison of the flux (top), spatial center ( $\chi_{Total}$ ; middle top), and seeing measured from the continuum ( $\sigma_{Total}$ ; bottom) of the IRS 48 CO lines from different observation dates. Black and blue are 2 Aug, 2008 at PA of 90 and 270 respectively (spatial center for 270° is multiplied by -1). Red is 5 September, 2007 and green is 3 May 2008.

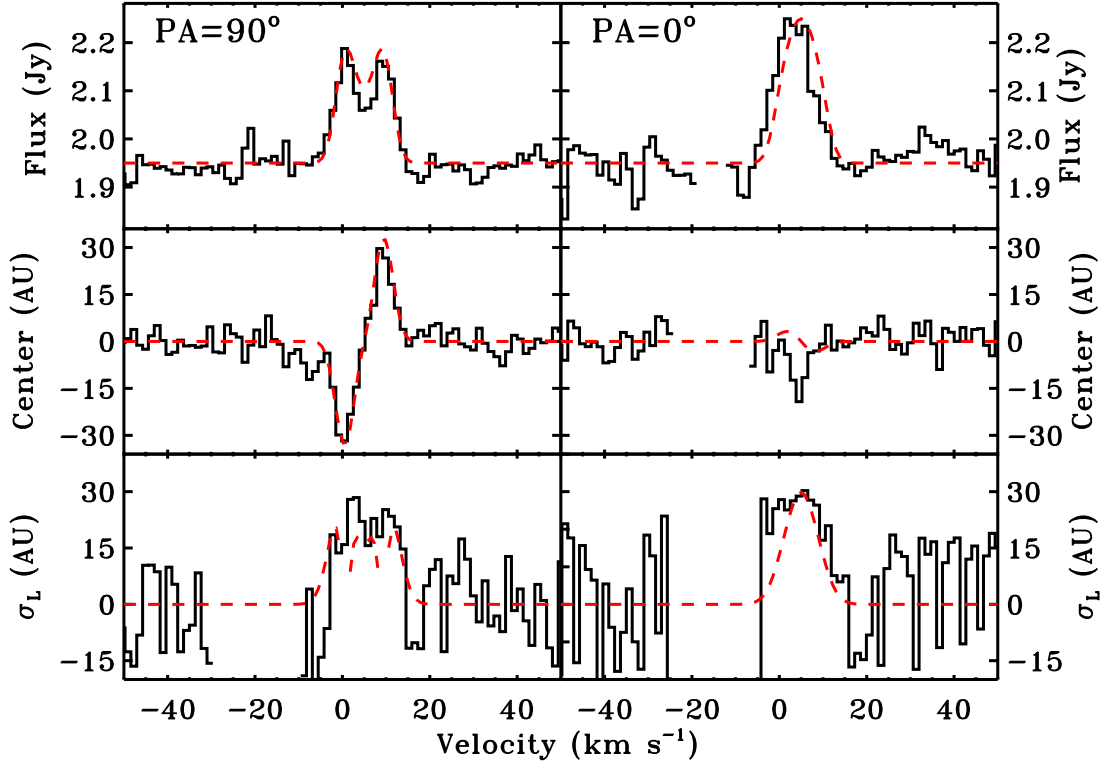


Fig. 8.— Comparison of the flux (top), spatial center (middle) and extent (bottom) of the IRS 48 CO lines. The left column is the spectroastrometry at position angles of  $90^\circ$  and  $270^\circ$  while the right column is  $0^\circ$  and  $180^\circ$ . The overplotted red line is a simple model of a ring of gas in Keplerian rotation at 30 AU around a  $2 M_\odot$  star with an inclination of  $42^\circ$ . The temperature of the disk outside this radius is taken to have a power-law distribution with an index of -0.6.

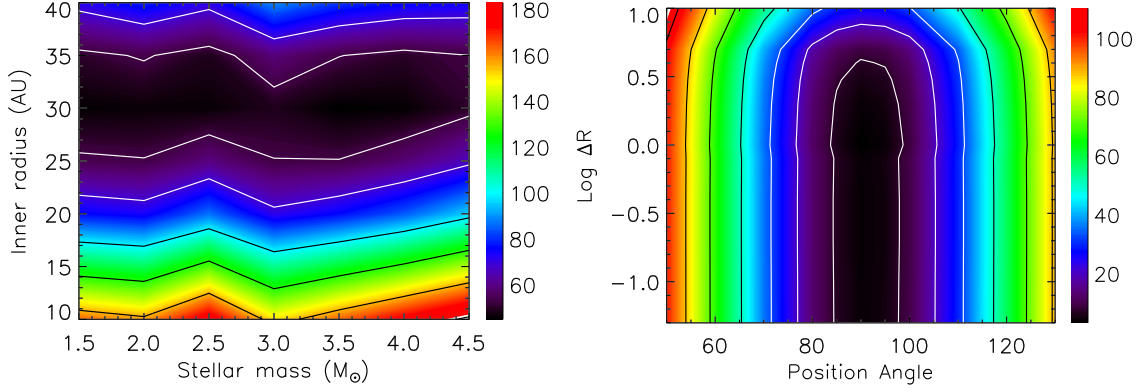


Fig. 9.— (left)  $\chi^2$  plot of  $R_0$  at each  $M$ , choosing the inclination and position angle which produce the best fits. The inclinations range from  $30^\circ$  to  $50^\circ$  with the higher masses tending to better fits at smaller inclinations.  $R_0$  is therefore fairly robust across a range of stellar masses. (right) The effects of varying emission region widths in a uniform temperature ring with constant density. The emission is clearly dominated by a small region close to  $R_0$ .

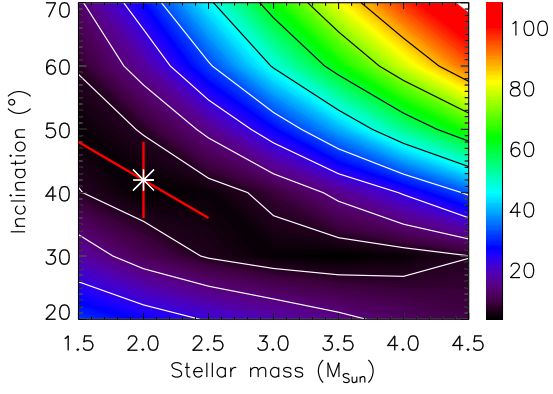


Fig. 10.—  $\chi^2$  plot of stellar mass vs inclination. The white star marks where the measured inclination of  $42^\circ$  is at the  $\chi^2$  minimum. The red vertical error bars show the error on the inclination while the diagonal line traces the lowest  $\chi^2$  values within the inclination errors.

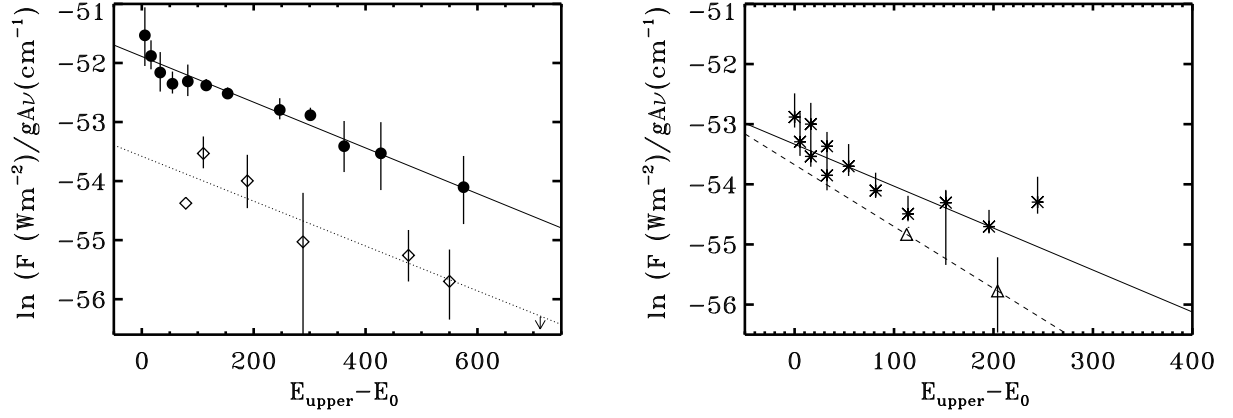


Fig. 11.— Rotation diagram of the CO emission lines. Filled circles are  $^{12}\text{CO}$ , diamonds are  $^{13}\text{CO}$  (dotted fit), stars are  $^{12}\text{CO}$  v=2-1, and triangles are  $^{12}\text{CO}$  v=3-2 (dashed fit). The energies refer to those of the rotational levels relative to J=0 in the respective vibrational state.

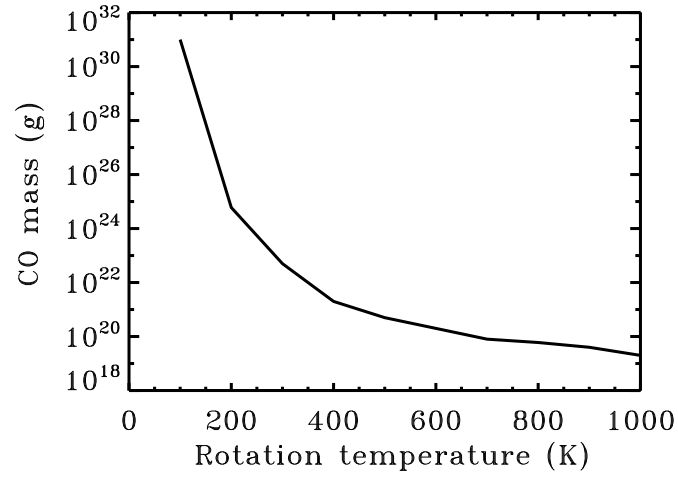


Fig. 12.— Upper limits on CO mass within the 30 AU hole assuming different gas temperatures.



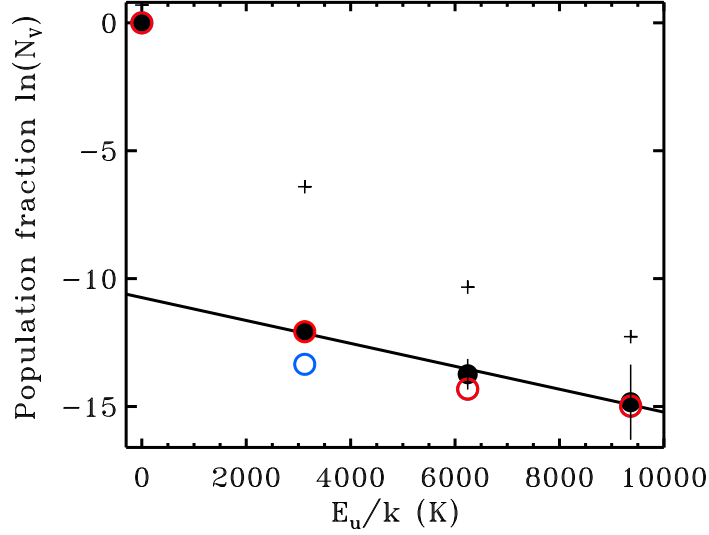


Fig. 13.— Vibrational diagram for IRS 48. The black points are the observed fractional population in each vibrational level. The linear fit indicates a vibrational temperature of 2200 K, greatly in excess of the rotation temperature of 260 K. The red circles are the expected vibrational fractions from a UV fluorescence model of IRS 48, including the thermal population. The blue circles, underlying the red for  $v > 1$ , are the vibrational component in each level before the collisionally excited population is added. The black crosses represent the expected excitation from our 1 Myr old, high mass spectral parameters with a luminosity of  $200 L_{\odot}$  at 30 AU. While the vibrationally excited emission increases by about an order of magnitude, the bulk of the increase is from the expected increase in collisional excitation with the increased temperature at 30 AU.

Table 1. Summary of CRIRES observations

Date	Wavelength (nm)	Position Angle	Number of Nod Cycles	Standard Star
2007 Sep 5	4730	90	1	HR 5812
2008 May 3	4730, 4833	90	2	HR 6084
2008 Aug 2	4710	0	3	HR 6084
2008 Aug 2	4730	0,90,180,270	3	HR 6084
2008 Aug 5	4868	90	3.5	HR 6175

Table 2. Model parameters

Parameter	Best fit model	Range
Hole size ( $R_0$ )	30 AU	25-35 AU
Stellar mass	2 $M_\odot$	1.5-2.5 $M_\odot$
Inclination	42°	36-48°
Position angle	95°	85°-100°
q	0.6	>0.4
$\Delta R$	1 AU	< 3 AU

Table 3. Summary of rotation diagrams<sup>1</sup>

Molecule	Rotational Temperature (K)	CO Mass (g)	CO Column Density (cm <sup>-2</sup> )
<sup>12</sup> CO v=1-0	256	7.2 10 <sup>23</sup>	7.2 10 <sup>17</sup>
<sup>13</sup> CO v=1-0	267	4.6 10 <sup>22</sup>	4.6 10 <sup>16</sup>
<sup>12</sup> CO v=2-1	204	–	–
<sup>12</sup> CO v=1-0	26	–	–
<sup>13</sup> CO v=1-0	17	–	–
C <sup>18</sup> O v=1-0	30	–	–

<sup>1</sup>Emission rotation diagram parameters are above the horizontal divide and absorption parameters are below.